

# Supplemental Material for: Magnetic excitations in $\text{Nd}_{n+1}\text{Ni}_n\text{O}_{3n+1}$ Ruddlesden-Popper nickelates observed via resonant inelastic x-ray scattering

Sophia F. R. TenHuisen,<sup>1,2</sup> Grace A. Pan,<sup>1</sup> Qi Song,<sup>1</sup> Denitsa R. Baykusheva,<sup>1</sup> Dan Ferenc Segedin,<sup>1</sup> Berit H. Goodge,<sup>3,4</sup> Hanjong Paik,<sup>5</sup> Jonathan Pelliciari,<sup>6</sup> Valentina Bisogni,<sup>6</sup> Yanhong Gu,<sup>6</sup> Stefano Agrestini,<sup>7</sup> Abhishek Nag,<sup>7</sup> Mirian García-Fernández,<sup>7</sup> Ke-Jin Zhou,<sup>7</sup> Lena F. Kourkoutis,<sup>3,4,\*</sup> Charles M. Brooks,<sup>1</sup> Julia A. Mundy,<sup>1</sup> Mark P. M. Dean,<sup>8,†</sup> and Matteo Mitrano<sup>1,‡</sup>

<sup>1</sup>*Department of Physics, Harvard University, Cambridge, MA, USA*

<sup>2</sup>*John A. Paulson School of Engineering and Applied Sciences, Harvard University, Cambridge, MA, USA*

<sup>3</sup>*School of Applied and Engineering Physics, Cornell University, Ithaca, NY, USA*

<sup>4</sup>*Kavli Institute at Cornell for Nanoscale Science, Cornell University, Ithaca, NY, USA*

<sup>5</sup>*Platform for the Accelerated Realization, Analysis and Discovery of Interface Materials (PARADIM), Cornell University, Ithaca, NY, USA*

<sup>6</sup>*National Synchrotron Light Source II, Brookhaven National Laboratory, Upton, New York 11973, USA*

<sup>7</sup>*Diamond Light Source, Harwell Campus, Didcot OX11 0DE, UK*

<sup>8</sup>*Condensed Matter Physics and Materials Science Department, Brookhaven National Laboratory, Upton, New York 11973, USA*

(Dated: April 8, 2025)

## S1. SAMPLE CHARACTERIZATION

Thin film  $\text{Nd}_{n+1}\text{Ni}_n\text{O}_{3n+1}$  samples on (001)-oriented  $\text{LaAlO}_3$  and (110)-oriented  $\text{NdGaO}_3$  were synthesized using reactive-oxide molecular-beam epitaxy according to the procedures described in Refs. [1, 2]. The synthesis process uses distilled ozone to reach a total chamber pressure of  $\sim 1-3 \times 10^{-6}$  and source materials of elemental neodymium and nickel evaporating with flux rates of  $\sim 1 \times 10^{13}$  atoms/cm<sup>2</sup>· s. The  $n = 3, 5$  compounds were synthesized with a substrate temperature of 660 - 690 °C and the  $n = 1$  compound at 1000 °C.

### A. X-ray diffraction

Thin film x-ray diffraction was performed on a Malvern Panalytical Empyrean diffractometer using  $\text{Cu K}\alpha_1$  radiation. Figure S1 displays the x-ray diffraction patterns for the four films considered in this study. All films exhibit sharp superlattice peaks, demonstrating the long-ranged structural order of the Ruddlesden-Popper motif. Reciprocal space maps (RSMs) of the compounds on  $\text{LaAlO}_3$  ( $a_{pc} = 3.79 \text{ \AA}$ ,  $\epsilon \approx -0.9\%$ ) and  $\text{NdGaO}_3$  ( $a_{pc} = 3.86 \text{ \AA}$ ,  $\epsilon \approx +1.0\%$ ), shown in Fig. S2, indicate that the samples in this study are largely strained to their substrates. The  $n = 1$  compound has partially relaxed to an intermediate strain state with  $a_{pc} \approx 3.835 \text{ \AA}$ . This could arise from the increased presence of rock salt layers, which may relieve the strain generated by external epitaxy [3].

### B. Electron microscopy

Specimens for cross-sectional scanning transmission electron microscopy (STEM) analysis were prepared using either a Thermo Fisher Scientific Helios G4 UX or an FEI Helios 660 focused ion beam (FIB), with a final thinning process performed at an energy of 2 keV. Aberration-corrected STEM imaging was conducted on a Thermo Fisher Scientific

\* Deceased

† mdean@bnl.gov

‡ mmmitrano@g.harvard.edu

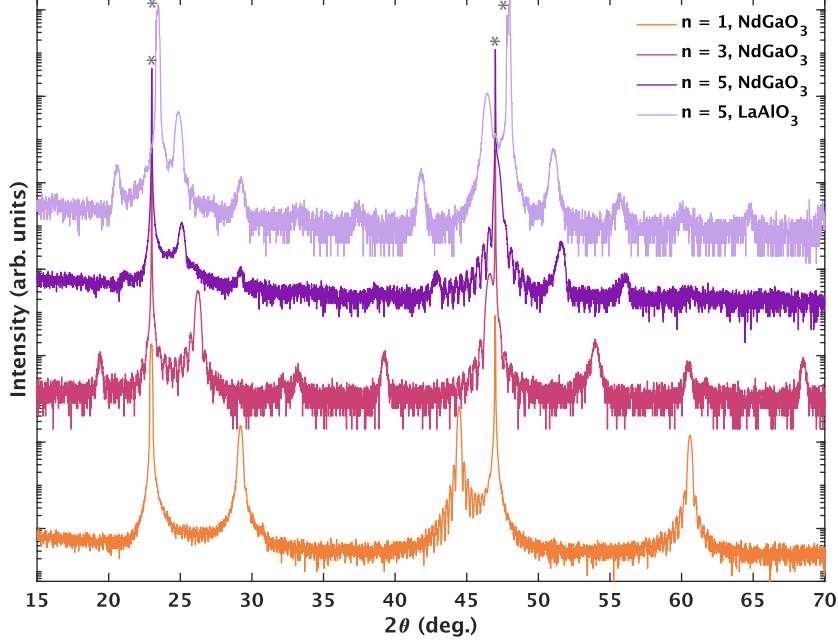


FIG. S1. X-ray diffraction patterns of the four  $\text{Nd}_{n+1}\text{Ni}_n\text{O}_{3n+1}$  thin film samples:  $n = 1$  on  $\text{NdGaO}_3$  (orange),  $n = 3$  on  $\text{NdGaO}_3$  (dark pink),  $n = 5$  on  $\text{NdGaO}_3$  (dark purple), and  $n = 5$  on  $\text{LaAlO}_3$  (light purple). Grey asterisks indicate substrate peaks. The  $n = 3$  on  $\text{NdGaO}_3$  and  $n = 5$  on  $\text{NdGaO}_3$  patterns are reproduced from Ref. [1].

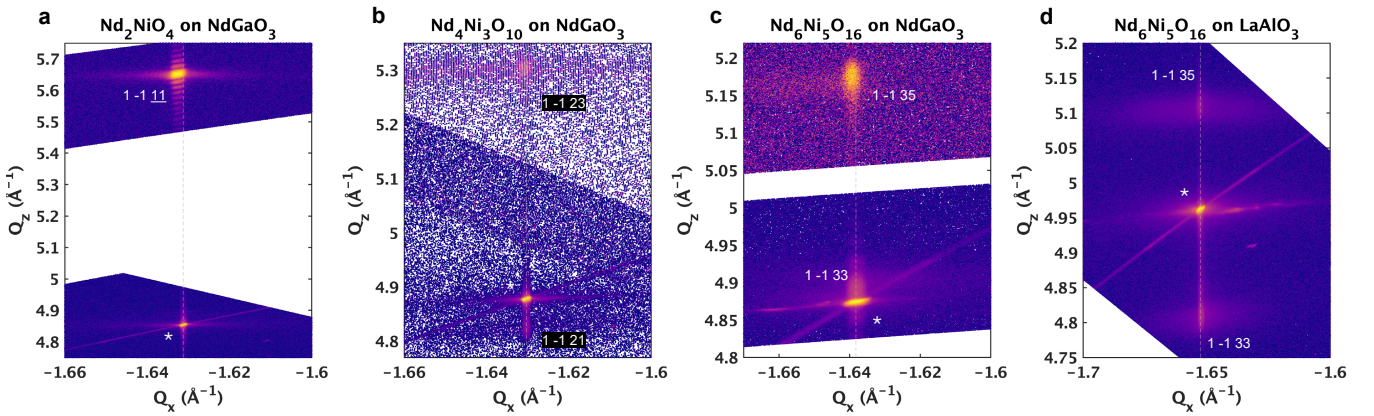


FIG. S2. Reciprocal space mapping of the four  $\text{Nd}_{n+1}\text{Ni}_n\text{O}_{3n+1}$  thin film samples. White asterisks indicate the  $3\ 3 -2$  peaks of  $\text{NdGaO}_3$  and  $-1\ 0\ 3$  peak of  $\text{LaAlO}_3$ . Film peaks are labeled directly on the maps. Grey dashed lines intersect the substrate peaks and are guides to the eye.

Spectra 300 X-FEG or Titan Themis CryoS/TEM microscope operating at 300 kV, using a probe convergence semi-angle of 30 mrad. High-angle annular dark-field (HAADF) STEM images were captured using collection angles ranging from 54 to 200 mrad.

Fig. S3 shows regions of the  $\text{Nd}_{n+1}\text{Ni}_n\text{O}_{3n+1}$  ( $n = 1, 3, 5$ ) thin films synthesized on  $\text{NdGaO}_3$ . The films have well-ordered, horizontally-stacked rock salt layers characteristic of the layered Ruddlesden-Popper phase. There are some regions of reduced contrast in the  $n = 3, 5$  films: rock salt regions which are offset by  $a/2[110]_{pc}$  will show up as areas of reduced atomic contrast due to the projection through mixed elemental species (neodymium, nickel) into the page. There are also some regions of locally varying  $n$  in the  $n = 5$  film, as the  $\text{Nd}_6\text{Ni}_5\text{O}_{16}$  compound is not synthesizable through bulk methods alone. Additional details of the microstructural characterization of these and related  $\text{Nd}_{n+1}\text{Ni}_n\text{O}_{3n+1}$  thin films may be found in Refs. [2, 3].

### C. Electronic transport

Electronic transport measurements as a function of temperature (Fig. S4) were taken down to 1.8 K using a Quantum Design Physical Property Measurement System (PPMS) using standard lock-in techniques at 15 Hz. Electrical resistivities were determined using devices in van der Pauw or Hall bar geometries. Contacts were patterned with shadow masks and deposited using an electron-beam evaporator (5 nm Cr/100 nm Au). Hall bar channels were defined with a diamond scribe.

The four films considered in this study have distinct transport properties. The  $\text{Nd}_2\text{NiO}_4$  film exhibits semiconducting behavior, consistent with bulk  $\text{Nd}_2\text{NiO}_4$  behavior [4]. The  $\text{Nd}_4\text{Ni}_3\text{O}_{10}$  film displays a resistivity kink at  $\sim 150$  K. Resistivity kinks have been attributed to density wave ordering in  $n = 2, 3 \text{ La}_{n+1}\text{Ni}_n\text{O}_{3n+1}$  [5–8], so the same behavior might be present in these  $\text{Nd}_3\text{Ni}_3\text{O}_{10}$  films. The two  $\text{Nd}_6\text{Ni}_5\text{O}_{16}$  films both exhibit hysteretic metal-insulator transitions. Under the application of compressive strain,  $\text{Nd}_6\text{Ni}_5\text{O}_{16}$  synthesized on  $\text{LaAlO}_3$  has a largely depressed metal-insulator transition temperature  $T_{MIT}$  and a lower resistivity scale. This may be potentially attributed to the straightening of Ni-O bonds by compressive strain and improved orbital overlap, which may have implications for superconductivity [9, 10], although the precise mechanism is unknown at this stage.

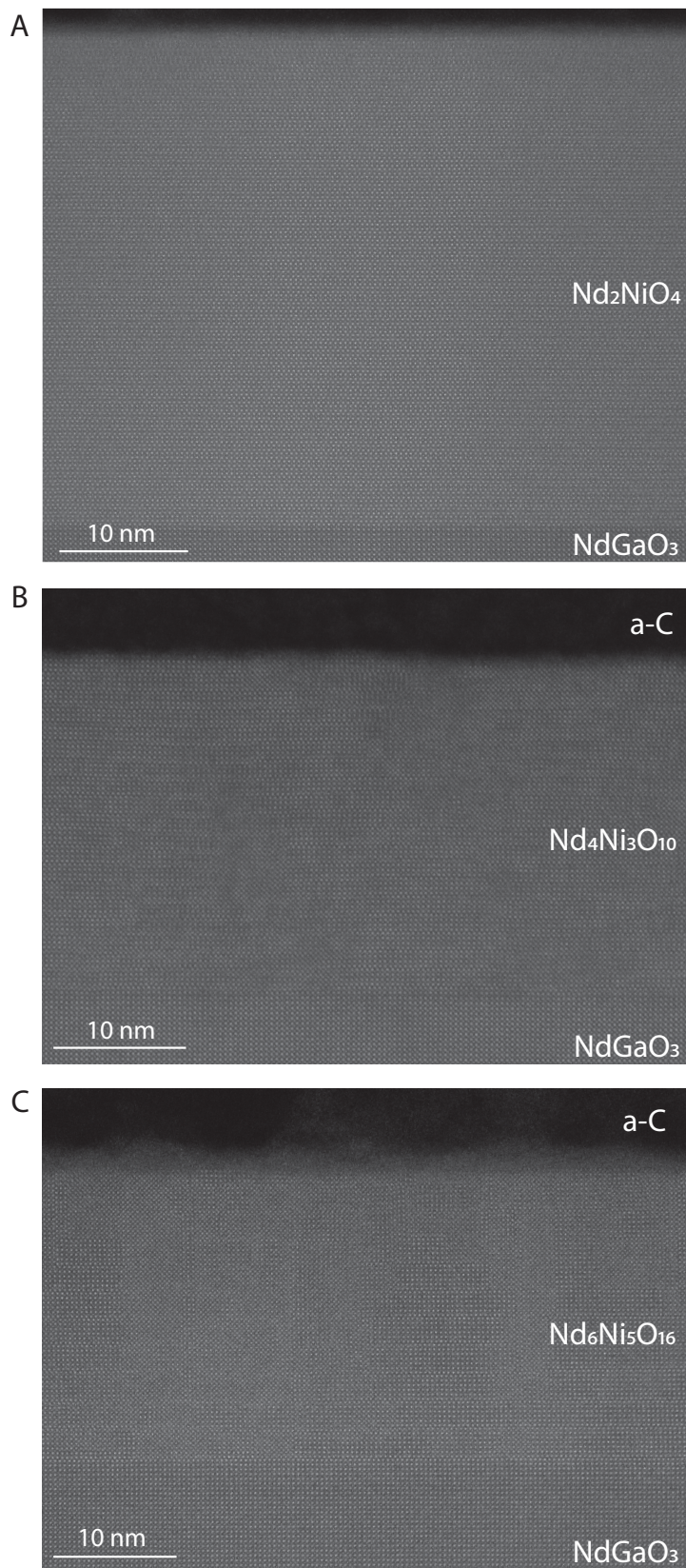


FIG. S3. Representative HAADF-STEM images of the (A)  $n = 1$ , (B)  $n = 3$ , and (C)  $n = 5$   $\text{Nd}_{n+1}\text{Ni}_n\text{O}_{3n+1}$  thin films synthesized on  $\text{NdGaO}_3$  substrates. a-C, amorphous carbon.

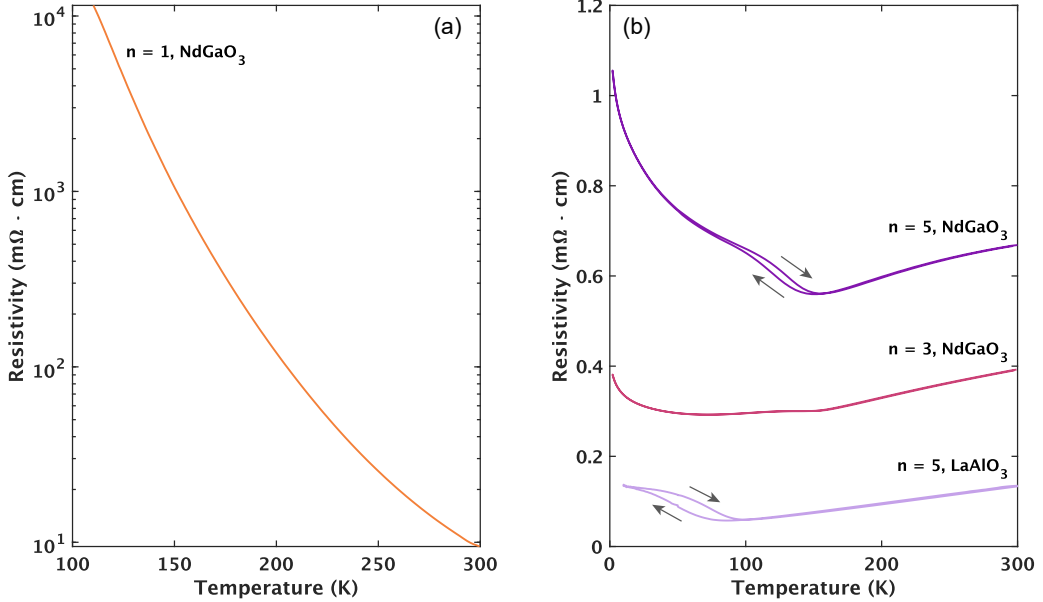


FIG. S4. Electrical transport behavior of the  $n = 1$  (a) and  $n = 3,5$  (b) films. Grey arrows indicate the direction of the temperature sweep for samples showing hysteretic behavior. The  $\text{Nd}_4\text{Ni}_3\text{O}_{10}$  and  $\text{Nd}_6\text{Ni}_5\text{O}_{16}$  traces are reproduced from Ref. [1].

## S2. ORBITAL EXCITATIONS

### A. Fluorescence and delocalized ligand states

Figure S5 shows the incident x-ray energy dependence of the resonant inelastic x-ray scattering (RIXS) across the  $\text{Ni } L_3$ -edge for  $\text{Nd}_6\text{Ni}_5\text{O}_{16}$  ( $n = 5$ ) and  $\text{Nd}_4\text{Ni}_3\text{O}_{10}$  ( $n = 3$ ). The spectra include both Raman-like features that occur at constant energy loss for different incident energies and fluorescent-like features which increase in energy with increasing incident x-ray energy. The fluorescence occurs when electrons from delocalized, itinerant states decay to fill the core-hole and implies the presence of ligand states that are hybridized with the resonant element [11]. As discussed in the main text, this indicates that the Ruddlesden-Popper nickelates adopt a  $|d^8 \underline{L}\rangle$  configuration, where  $\underline{L}$  denotes the hybridized oxygen ligand band [12, 13].

### B. Minimal orbital polarization

One key difference between Ruddlesden-Popper nickelates compared with the cuprates and square-planar nickelates is that Ruddlesden-Popper nickelates are expected to have much weaker orbital polarization. We tested for orbital polarization in the higher  $n$  Ruddlesden-Popper films by measuring the incident polarization dependence of orbital excitations near grazing incidence ( $\theta = 16^\circ$ ) as shown in Fig. S6. At this angle, horizontal ( $\pi$ ) polarized light primarily probes the out-of-plane  $d_{3z^2-r^2}$  orbital while vertical ( $\sigma$ ) polarized light primarily probes the in-plane  $d_{x^2-y^2}$  orbital. The orbital excitations show minimal incident polarization dependence, indicating that holes are distributed roughly equally between both the in-plane and out-of-plane  $e_g$  orbitals. For comparison, we also show the orbital dichroism in  $\text{Nd}_2\text{NiO}_4$  ( $n = 1$ ), which is measured by comparing  $\pi$ -polarized RIXS taken near grazing incidence ( $\theta = 16^\circ$ ) and near normal incidence ( $\theta = 72^\circ$ ), normalized to the integrated orbital intensities.

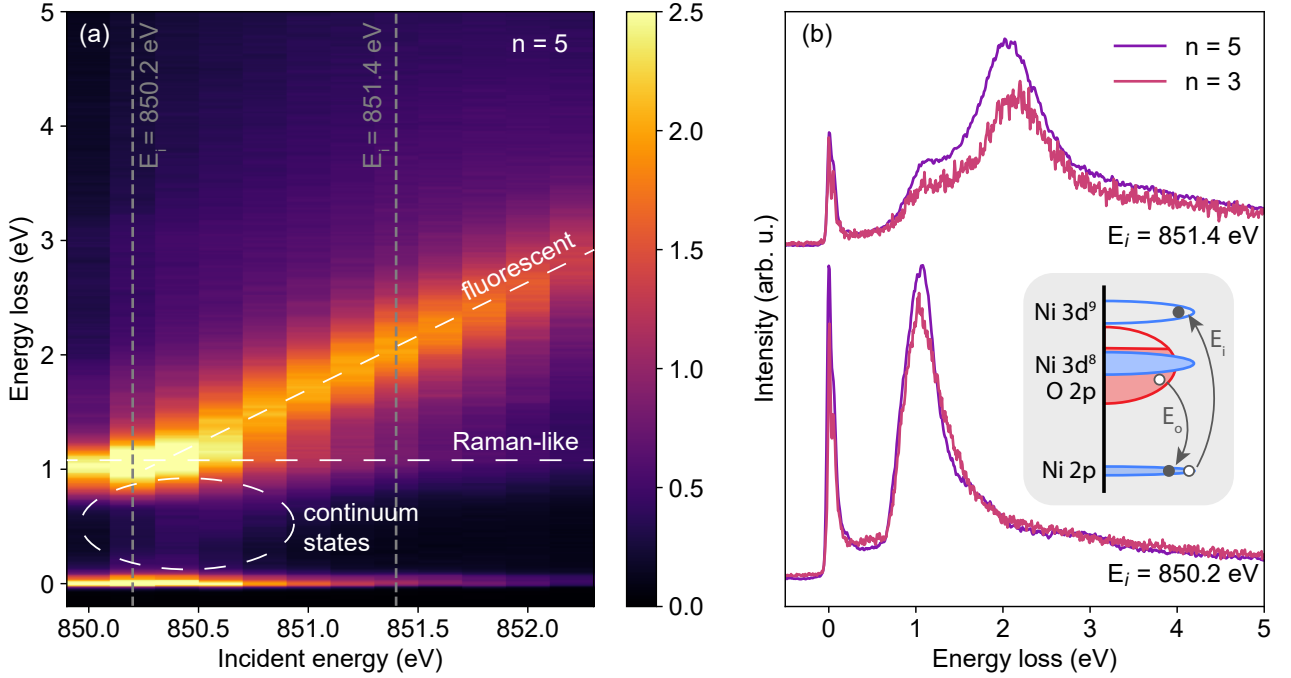


FIG. S5. Fluorescent orbital excitations in  $\text{Nd}_6\text{Ni}_5\text{O}_{16}$  ( $n = 5$ ) and  $\text{Nd}_4\text{Ni}_3\text{O}_{10}$  ( $n = 3$ ). A) Incident-energy dependence of orbital RIXS excitations in  $\text{Nd}_6\text{Ni}_5\text{O}_{16}$ . Fluorescent features appear at increasing energy loss as incident energy is increased, while Raman-like features appear at fixed energy loss. B) Comparison of orbital RIXS features in  $\text{Nd}_6\text{Ni}_5\text{O}_{16}$  and  $\text{Nd}_4\text{Ni}_3\text{O}_{10}$  at selected incident energies, highlighting the similar behavior between the two materials. The inset shows the fluorescent RIXS process, in which states from delocalized, hybridized orbitals dominate the decay channel.  $E_i$  denotes the incident x-ray photon while  $E_o$  denotes the emitted x-ray photon.

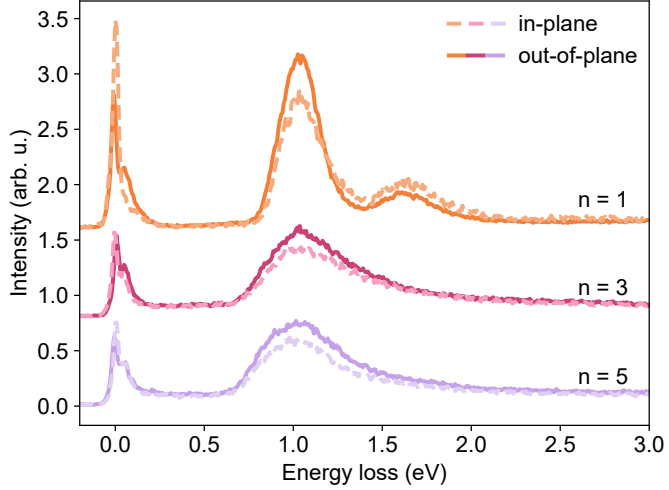


FIG. S6. Orbital dichroism of RIXS for  $\text{Nd}_2\text{NiO}_4$  ( $n = 1$ ) on  $\text{NdGaO}_3$  (orange),  $\text{Nd}_4\text{Ni}_3\text{O}_{10}$  ( $n = 3$ ) on  $\text{NdGaO}_3$  (pink), and  $\text{Nd}_6\text{Ni}_5\text{O}_{16}$  ( $n = 5$ ) on  $\text{LaAlO}_3$  (purple). RIXS dominantly probing in-plane orbitals is shown with a dashed line and RIXS probing dominantly out-of-plane orbitals is shown with a solid line. For  $\text{Nd}_2\text{NiO}_4$  the in-plane orbitals are probed with  $\pi$ -polarized light near normal incidence ( $\theta = 72^\circ$ ) and out-of-plane orbitals are probed with  $\pi$ -polarized light near grazing incidence ( $\theta = 16^\circ$ ). For  $\text{Nd}_4\text{Ni}_3\text{O}_{10}$  and  $\text{Nd}_6\text{Ni}_5\text{O}_{16}$ , in-plane orbitals are probed with  $\sigma$ -polarized light near grazing incidence ( $\theta = 16^\circ$ ) and out-of-plane orbitals are probed with  $\pi$ -polarized light near grazing incidence ( $\theta = 16^\circ$ ).

### S3. MODIFICATION TO MAGNETIC DISPERSION FROM LINEAR SPIN-WAVE THEORY

We use the package Sunny [14] to model the expected magnetic dispersions with increasing  $n$  within linear spin-wave theory (LSWT). For all samples we fix the in-plane magnetic exchange to  $J = 16$  meV, matching the magnon bandwidth for our measurements on  $\text{Nd}_2\text{NiO}_4$  ( $n = 1$ ). We show the calculated magnon dispersion overlaid with the data in Fig. S7. For higher  $n$  we include an out-of-plane magnetic exchange between  $n$  adjacent Ni layers, with  $J_z = J$ , assuming a symmetric octahedral environment. As shown in Fig. S8, as  $n$  is increased, an additional magnon branch emerges for each additional Ni layer. Furthermore, the energies of the magnetic excitations are shifted to higher energies due to the introduction of the additional magnetic exchange pathway.

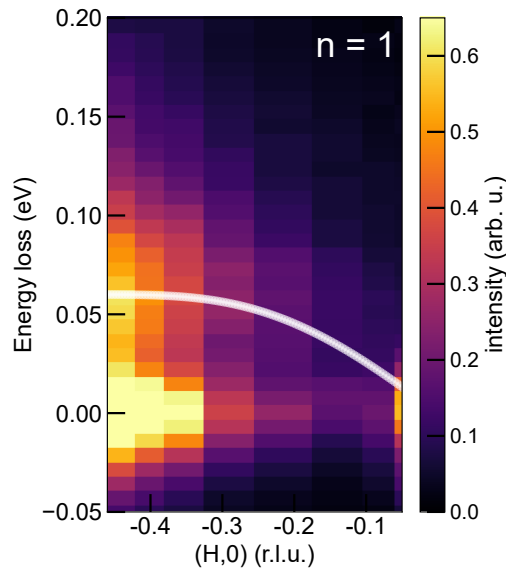


FIG. S7. RIXS data for  $\text{Nd}_2\text{NiO}_4$  ( $n = 1$ ) overlaid with the calculated dispersion from LSWT calculated with  $J = 16$  meV.

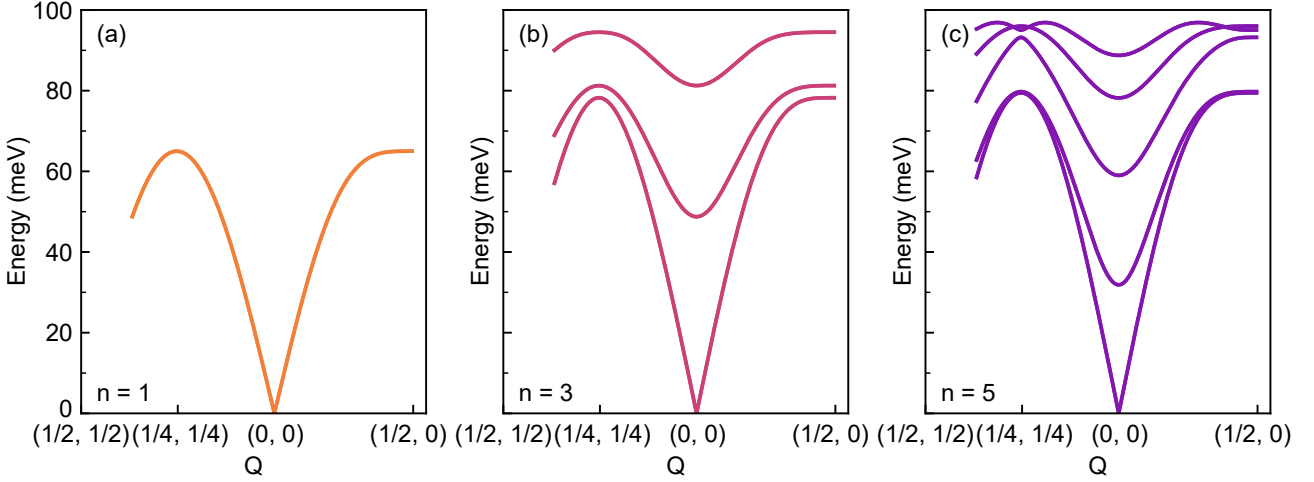


FIG. S8. LSWT calculations for magnetic branches for a material with a) a single layer, b) 3 layers, and c) 5 layers in a unit cell, with in-plane exchange  $J = 16$  meV. For the 3- and 5-layer cases, the out-of-plane exchange  $J_z$  is set equal to the in-plane exchange.

#### S4. STRAIN DEPENDENCE OF $\text{Nd}_6\text{Ni}_5\text{O}_{16}$ ( $n = 5$ )

Here we show the strain imparted by the substrate has minimal impact on the orbital and magnetic features reported in the main text by comparing RIXS spectra for  $\text{Nd}_6\text{Ni}_5\text{O}_{16}$  ( $n = 5$ ) synthesized on two different substrates. Films synthesized on  $\text{LaAlO}_3$  experience a small amount of compressive strain ( $\epsilon \approx -0.9\%$ ), while those on  $\text{NdGaO}_3$  discussed in the main text experience tensile strain ( $\epsilon \approx +1.0\%$ ). As  $\text{Nd}_6\text{Ni}_5\text{O}_{16}$  ( $n = 5$ ) can only be synthesized in thin-film form, strain values are approximated using bulk lattice constants for  $\text{Nd}_4\text{Ni}_3\text{O}_{10}$  ( $n = 3$ ) [15]. Based on the resistivity in Sec. S1 C, compressive strain suppresses the metal-insulator transition to lower temperatures and increases the conductivity of the samples overall but does not otherwise substantially affect the key findings reported in the main text.

Strain appears to have a limited impact on the magnetic features in  $\text{Nd}_6\text{Ni}_5\text{O}_{16}$  along  $[H, 0]$ . This suggests that the Ni-O exchange probed by this reciprocal space cut is minimally sensitive to strain, similar to what has been observed in thin films of perovskite  $\text{NdNiO}_3$  [16] and infinite-layer square-planar nickelates [17].

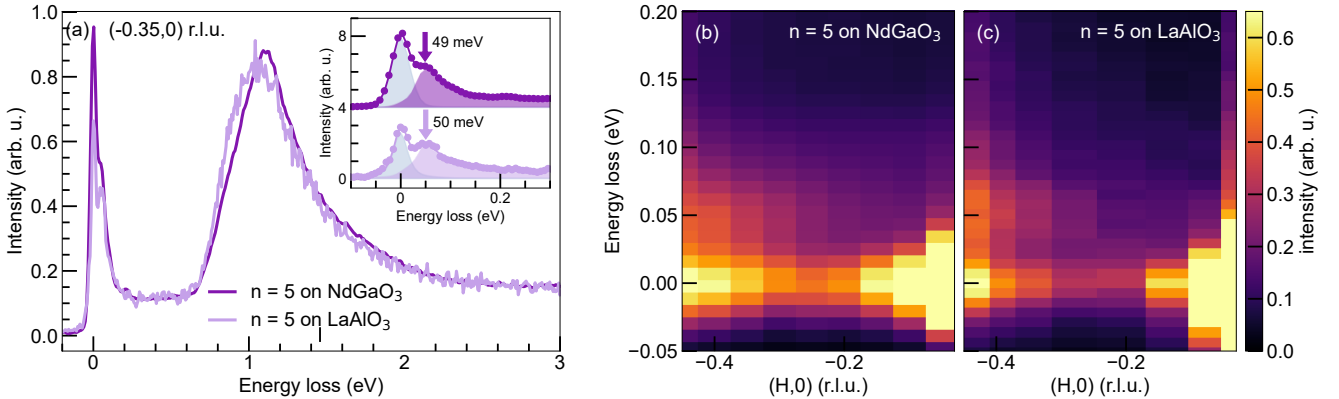


FIG. S9. Impact of strain on RIXS spectra. A) RIXS spectra for  $\text{Nd}_6\text{Ni}_5\text{O}_{16}$  on  $\text{NdGaO}_3$  (tensile) and on  $\text{LaAlO}_3$  (compressive). The inset shows a zoom-in on the magnetic portion of the RIXS spectra, showing similar magnetic peak positions in both samples. B) Momentum dependence of magnetic excitations in  $\text{Nd}_6\text{Ni}_5\text{O}_{16}$  on  $\text{NdGaO}_3$  (tensile) along  $[H, 0]$  (reproduced from main). C) Momentum dependence of magnetic excitations in  $\text{Nd}_6\text{Ni}_5\text{O}_{16}$  on  $\text{LaAlO}_3$  (compressive) along  $[H, 0]$ .

- 
- [1] G. A. Pan, D. Ferenc Segedin, H. LaBollita, Q. Song, E. M. Nica, B. H. Goodge, A. T. Pierce, S. Doyle, S. Novakov, D. Córdova Carrizales, *et al.*, Superconductivity in a quintuple-layer square-planar nickelate, *Nat. Mater.* **21**, 160 (2022).
- [2] G. A. Pan, Q. Song, D. Ferenc Segedin, M.-C. Jung, H. El-Sherif, E. E. Fleck, B. H. Goodge, S. Doyle, D. Córdova Carrizales, A. T. N'Diaye, P. Shafer, H. Paik, L. F. Kourkoutis, I. El Baggari, A. S. Botana, C. M. Brooks, and J. A. Mundy, Synthesis and electronic properties of  $\text{Nd}_{n+1}\text{Ni}_n\text{O}_{3n+1}$  Ruddlesden-Popper nickelate thin films, *Phys. Rev. Mater.* **6**, 055003 (2022).
- [3] D. Ferenc Segedin, B. H. Goodge, G. A. Pan, Q. Song, H. LaBollita, M.-C. Jung, H. El-Sherif, S. Doyle, A. Turkiewicz, N. K. Taylor, *et al.*, Limits to the strain engineering of layered square-planar nickelate thin films, *Nat. Commun.* **14**, 1468 (2023).
- [4] Y. Takeda, M. Nishijima, N. Imanishi, R. Kanno, O. Yamamoto, and M. Takano, Crystal chemistry and transport properties of  $\text{Nd}_{2-x}\text{A}_x\text{NiO}_4$  ( $A = \text{Ca}, \text{Sr}, \text{or Ba}, 0 \leq x \leq 1.4$ ), *J. Solid State Chem.* **96**, 72 (1992).
- [5] X. Chen, J. Choi, Z. Jiang, J. Mei, K. Jiang, J. Li, S. Agrestini, M. Garcia-Fernandez, H. Sun, X. Huang, D. Shen, M. Wang, J. Hu, Y. Lu, K. J. Zhou, and D. Feng, Electronic and magnetic excitations in  $\text{La}_3\text{Ni}_2\text{O}_7$ , *Nat. Commun.* **15**, 9597 (2024).
- [6] N. K. Gupta, R. Gong, Y. Wu, M. Kang, C. T. Parzyck, B. Z. Gregory, N. Costa, R. Sutarto, S. Sarker, A. Singer, D. G. Schloss, K. M. Shen, and D. G. Hawthorn, Anisotropic spin stripe domains in bilayer  $\text{La}_3\text{Ni}_2\text{O}_7$  (2024), [arXiv:2409.03210](#).
- [7] X. Ren, R. Sutarto, X. Wu, J. Zhang, H. Huang, T. Xiang, J. Hu, R. Comin, X. J. Zhou, and Z. Zhu, Resolving the electronic ground state of  $\text{La}_3\text{Ni}_2\text{O}_{7-\delta}$  films, *Commun Phys* **8**, 52 (2025).
- [8] J. Zhang, D. Phelan, A. S. Botana, Y.-S. Chen, H. Zheng, M. Krogstad, S. G. Wang, Y. Qiu, J. Rodriguez-Rivera, R. Osborn, S. Rosenkranz, M. R. Norman, and J. F. Mitchell, Intertwined density waves in a metallic nickelate, *Nat. Commun.* **11**, 6003 (2020).
- [9] S. Catalano, M. Gibert, J. Fowlie, J. Iniguez, J.-M. Triscone, and J. Kreisel, Rare-earth nickelates  $R\text{NiO}_3$ : thin films and heterostructures, *Rep. Prog. Phys.* **81**, 046501 (2018).
- [10] L. Bhatt, A. Y. Jiang, E. K. Ko, N. Schnitzer, G. A. Pan, D. F. Segedin, Y. Liu, Y. Yu, Y.-F. Zhao, E. A. Morales, *et al.*, Resolving structural origins for superconductivity in strain-engineered  $\text{La}_3\text{Ni}_2\text{O}_7$  thin films (2025).
- [11] M. Mitrano, S. Johnston, Y.-J. Kim, and M. P. M. Dean, Exploring quantum materials with resonant inelastic x-ray scattering, *Phys. Rev. X* **14**, 040501 (2024).
- [12] M. R. Norman, A. S. Botana, J. Karp, A. Hampel, H. Labollita, A. J. Millis, G. Fabbri, Y. Shen, and M. P. M. Dean, Orbital polarization, charge transfer, and fluorescence in reduced-valence nickelates, *Phys. Rev. B* **107**, 165124 (2023).
- [13] Y. Shen, J. Sears, G. Fabbri, J. Li, J. Pelliciari, M. Mitrano, W. He, J. Zhang, J. F. Mitchell, V. Bisogni, M. R. Norman, S. Johnston, and M. P. M. Dean, Electronic character of charge order in square-planar low-valence nickelates, *Phys. Rev. X* **13**, 011021 (2023).
- [14] D. Dahlbom, H. Zhang, C. Miles, S. Quinn, A. Niraula, B. Thipe, M. Wilson, S. Matin, H. Mankad, S. Hahn, D. Pajerowski, S. Johnston, Z. Wang, H. Lane, Y. W. Li, X. Bai, M. Mourigal, C. D. Batista, and K. Barros, *Sunny.jl: A julia package for spin dynamics* (2025), [arXiv:2501.13095](#).
- [15] Q. Li, C. He, X. Zhu, J. Si, X. Fan, and H.-H. Wen, Contrasting physical properties of the trilayer nickelates  $\text{Nd}_4\text{Ni}_3\text{O}_{10}$  and  $\text{Nd}_4\text{Ni}_3\text{O}_8$ , *Sci. China Phys. Mech. Astron.* **64**, 227411 (2020).
- [16] K. Fürsich, Y. Lu, D. Betto, M. Bluschke, J. Porras, E. Schierle, R. Ortiz, H. Suzuki, G. Cristiani, G. Logvenov, N. B. Brookes, M. W. Haverkort, M. Le Tacon, E. Benckiser, M. Minola, and B. Keimer, Resonant inelastic x-ray scattering study of bond order and spin excitations in nickelate thin-film structures, *Phys. Rev. B* **99**, 165124 (2019).
- [17] Q. Gao, S. Fan, Q. Wang, J. Li, X. Ren, I. Bialo, A. Drewnowski, P. Rothenbühler, J. Choi, R. Sutarto, Y. Wang, T. Xiang, J. Hu, K. J. Zhou, V. Bisogni, R. Comin, J. Chang, J. Pelliciari, X. J. Zhou, and Z. Zhu, Magnetic excitations in strained infinite-layer nickelate  $\text{PrNiO}_2$  films, *Nat. Commun.* **15**, 5576 (2024).